

Tissue-Engineered Bone Functionalized with MoS₂ Nanosheets for Enhanced Repair of Critical-Size Bone Defect in Rats

Jie Zhang, Boyou Zhang, Zefeng Zheng, Qingyun Cai, Jingcheng Wang,* Qiang Shu,* and Lijia Wang*

Tissue-engineered bones have therapeutic potential for critical-size bone defects; however, the production of high quantities of the tissue-engineered bones with osteo-induction ability remains a huge challenge. Hyperthermia has been shown to up-regulate the expression of osteogenesis-related proteins to efficiently to promote bone regeneration. In this study, the authors develop a novel photothermal tissueengineered bone (PTEB) with osteo-induction ability and a biomimetic cellular environment. PTEB is generated by seeding rat bone mesenchymal stem cells (rBMMSCs) in the photothermal MoS₂-biotin-garose-gelatin scaffold, and then overlaying the scaffold using osteo-induction extracellular matrix (OiECM). The rBMMSCs act as seeding cells, while OiECM provide a biomimetic microenvironment for repairing critical-sized cranial defects in rats. The results show that the PTEB exhibit high biocompatibility and osteo-induction ability under near-infrared (NIR) radiation. Results of in vitro experiments show that PTEB under NIR radiation promote proliferation and osteogenic differentiation of rBMMSCs. Furthermore, the PTEB implantation under NIR radiation significantly induces regeneration of bone in critical-size bone defects in rats 12 weeks after implantation. These findings indicate that PTEB has great potential in regenerative medicine and may represent an effective replacement for autografts used commonly in bone tissue engineering.

1. Introduction

Critical-size bone defects are the smallest bone defects that do not heal themselves during the lifetime of an animal. Congenital malformations, arthritis, severe trauma, and surgical resection of malignant bone tumors may lead to critical-size bone defects.^[1] To restore the physiological functions of bones with critical-size defects, surgeons need to timely and effectively replace the defective bone structure with implants during reconstruction and repair surgeries.^[2] Since the implants commonly used lack osteo-induction ability, the clinical outcomes of bone repair are often unsatisfactory. At present, autograft and allograft tissue-engineered bone have become a promising approach for repairing critical-size bone defects.^[3,4] However, the supply of tissue-engineered bone is limited by donor shortage or immunogenicity. Therefore, there is urgent need to increase the production of

J. Zhang, J. Wang
Department of Orthopedics
The Second Xiangya Hospital
Central South University
Changsha, Hunan 410011, China
E-mail: jcwang@yzu.edu.cn


J. Zhang, L. Wang
The Children's Hospital
Zhejiang University School of Medicine
National Clinical Research Center for Child Health
National Children's Regional Medical Center
Hangzhou, Zhejiang 310052, China
E-mail: wanglijia@zju.edu.cn

B. Zhang
Department of Thoracic Surgery
The Second Xiangya Hospital
Central South University
Changsha, Hunan 410011, China

Z. zheng, Q. Shu
Department of Pediatric Surgery
The Children's Hospital
Zhejiang University School of Medicine
National Clinical Research Center for Child Health
Hangzhou, Zhejiang 310052, China
E-mail: Shuqiang@zju.edu.cn

Q. Cai
State Key Laboratory of Chemo/Biosensing & Chemometrics
College of Chemistry & Chemical Engineering
Hunan University
Changsha, Hunan 410082, China

J. Wang
Department of Orthopedics
Northern Jiangsu People's Hospital Affiliated to Yangzhou University
Yangzhou, Jiangsu 225001, China

 The ORCID identification number(s) for the author(s) of this article can be found under <https://doi.org/10.1002/adfm.202109882>.

DOI: 10.1002/adfm.202109882

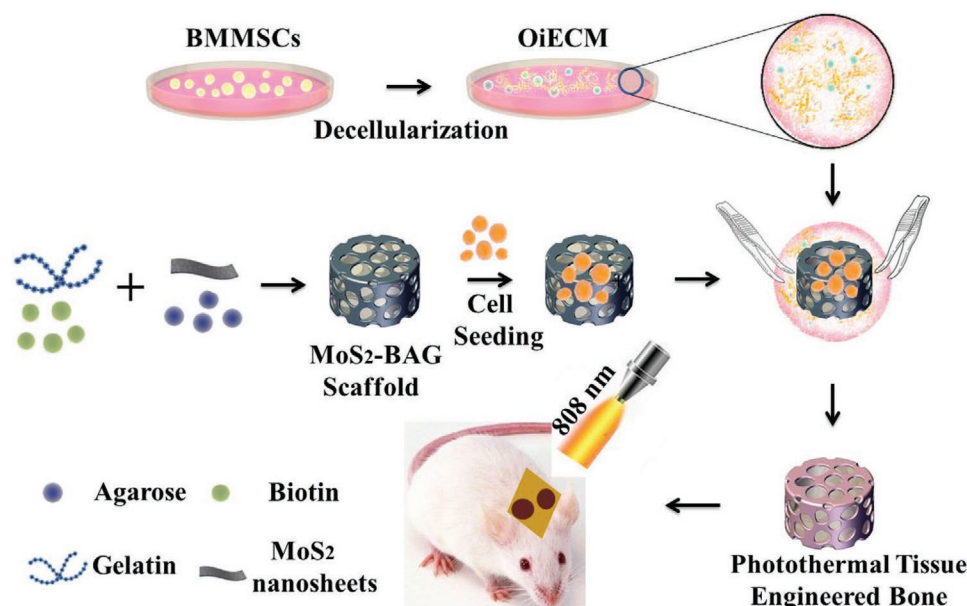
tissue-engineered bone with osteo-induction ability for clinical applications.

The foundation of bone tissue engineering based on the proliferation and differentiation of rat bone mesenchymal stem cells (rBMMSCs). So, it is of great significance to select an appropriate matrix to provide a good microenvironment for rBMMSCs. Recently, bone marrow mesenchymal stem cells (BMMSCs)-derived extracellular matrix (ECM) has attracted a lot of attention. This is because the ECM can create biomimetic cellular environments and contains a lot of cell-secreted growth factors that enhance cell growth and response.^[3–6] Zhang et al. reported that an extracellular matrix in the collagen scaffolds enhanced cell recruitment, proliferation, and chondrogenesis of BMMSCs in vitro, providing a more favorable chondrogenic microenvironment for endogenous BMMSCs.^[7] Yoo et al. demonstrated that a protein-reactive nanofiber decorated with extracellular matrix mimics the structural and biochemical properties of a cartilage-specific microenvironment and facilitated the reconstruction of their cartilage and subchondral bone ECM matrices.^[8] Oreffo et al. reported that a bovine extracellular matrix (bECM) hydrogel modified polycaprolactone scaffold efficiently induced bone formation in a critical-sized ovine segmental tibial defect model.^[9] Implantation of medical devices with poor biocompatibility induces chronic inflammation, tissue injury, and tissue fibrosis in the host, leading to the rejection of the implant or rendering it ineffective.^[10] To prevent immune rejection from seeded cells and host tissues, the ECM can be decellularized to get rid of cellular and genetic material. Decellularized ECM (dECM) is a 3D network of fibers that retain the tissue-specific structural and biological function of the ECM.

Recent studies have shown that gentle photothermal radiation can promote osteogenesis by up-regulating the expression of alkaline phosphatase (ALP) and heat shock proteins (HSP).^[11–17] Wang et al. found that the osteo implant of BPs@PLGA efficiently promoted osteogenesis under near-infrared (NIR) light

radiation.^[18] Wu et al. reported that the excellent photothermal characteristics of BG-CFS scaffolds modified with CuFeSe₂ nanocrystals could stimulate the expression of osteogenic genes in bone marrow stromal cells and finally facilitate the formation of new bone in the bone defects.^[19] Shen et al. prepared carbon dot/WS₂ heterojunctions which generate effective photothermal effects in the NIR window, and enhance tissue regeneration effectively.^[20] The photothermal agents are activated in the NIR window allowing for high photothermal conversion rate and deep-tissue penetration efficiency.^[21] Therefore, it is important that the photothermal agents are effectively activated in the NIR window to maximize the photothermal effects for promoting osteogenesis in deep tissues when applied in bone tissue engineering. Molybdenum disulfide (MoS₂) nanosheets are an emerging class of layered 2D metal dichalcogenides with excellent biocompatibility and photothermal conversion efficiency under 808 nm irradiation.^[22–30] These characteristics indicate that MoS₂ biomaterials have great potential for promoting biomineralization and achieving bone remodeling.^[31–33]

The aim of this study was to develop a strategy to increase the production of tissue-engineered bone with osteo-induction ability. To achieve this, we combined osteo-inductive extracellular matrix (OiECM) and MoS₂ nanosheets to generate photothermal tissue-engineered bone (PTEB) with osteo-induction ability. In this study, we generated a PTEB made of MoS₂-biotin-agarose-gelatin scaffold and OiECM for promoting bone regeneration. **Scheme 1** shows the schematic diagram of enhanced osteogenic differentiation by PTEB under NIR laser irradiation and the related mechanism was discussed further. During the generation process, we first combined the MoS₂ nanosheets with excellent photothermal properties with a bio-friendly (biotin-agarose-gelatin) BAG scaffold to form a MoS₂-BAG scaffold.^[34–36] Thereafter, we seeded MoS₂-BAG scaffold with BMMSCs and then covered the scaffold with OiECM to generate a PTEB. Results of in vitro and in vivo assays conducted 12-weeks after implantation showed that the PTEB with



Scheme 1. Schematic illustration of the fabrication of photothermal tissue-engineered bone and their repairing the critical-size bone defect model in rats.

or without NIR radiation had the greatest effect on repairing the critical-size bone defect in a rat model.

2. Results and Discussion

2.1. Preparation and Characterizations of PTEB

2.1.1. Preparation and Characterizations of MoS₂ Nanosheets

The novel PTEB was generated by seeding the photothermal MoS₂-BAG scaffold with rBMSCs, followed by overlaying the scaffold with OiECM. The rBMSCs acted as seeding cells, while OiECM provided a biomimetic microenvironment. MoS₂ nanosheets were synthesized using the solvent-based exfoliation method. As shown in **Figure 1A,B**, the MoS₂ nanosheets had 2D structure with the size $\approx 270 \pm 60$ nm. **Figure 1C** shows that the MoS₂ nanosheets shows excellent biocompatibility with rBMSCs, even at the high concentration of 200 $\mu\text{g mL}^{-1}$. **Figure 1D** shows the X-ray diffraction (XRD) patterns of the MoS₂ nanosheets with the peaks exhibited at angle $2\theta = 14.3^\circ$ being consistent with the crystal plane (002). Results of Raman spectra analysis of the MoS₂ nanosheets showed one sharp MoS₂ Raman signal at 378 cm^{-1} , which was assigned to in-plane E_{2g}^1 mode and another sharp Raman signal 403 cm^{-1} , which was assigned to out-of-plane A_{1g} vibration mode (**Figure 1E**). These signals were consistent with previous reports on the features of the monolayer MoS₂ nanosheets.^[37,38] **Figure 1F** shows the photothermal heating curves of the MoS₂ nanosheets solution and phosphate buffered solution (PBS) under 808 nm laser radiation (1.0 W cm^{-2}). The temperature of MoS₂ nanosheets solution

increased significantly with time, while the temperature of PBS solution showed no obvious change. The MoS₂ nanosheets solution attained a maximum temperature of 46.1 $^\circ\text{C}$, indicating that the MoS₂ nanosheets can act as a good photothermal agent.

2.1.2. Preparation and Characterizations of OiECM

OiECM can promote osteogenesis differentiation of BMSCs by mimicking the natural biological environment for the stem cells. OiECM was obtained by culturing rat BMSCs isolated from 2-weeks Sprague-Dawley rats in osteo-inductive culture medium for 21 days. The cells displayed fibroblast-like characteristics after 2 weeks in culture (**Figure S1A**, Supporting Information). To ensure that we had isolated the right cells, we investigated the trilineage differentiation potential of the cells. The BMSCs were successfully stained with alizarin red, indicating the presence of calcium nodules and that the BMSCs were undergoing for osteogenic differentiation (**Figure S1B**, Supporting Information). The BMSCs also stained for the accumulation of lipid vacuoles in the cytoplasm after oil red O staining, indicating that the BMSCs were undergoing adipogenic differentiation (**Figure S1C**, Supporting Information). Finally, we demonstrated the ability of the BMSCs to differentiate into the chondrogenic lineage by culturing the cells in the chondrogenic induction agent and staining with safranin O (**Figure S1D**, Supporting Information). These results showed that we had successfully isolated the rat BMSCs.

To prevent immune rejection from seeded cells and host tissues, the ECM was decellularized to get rid of cellular and genetic material. OiECM was obtained by removing BMSCs

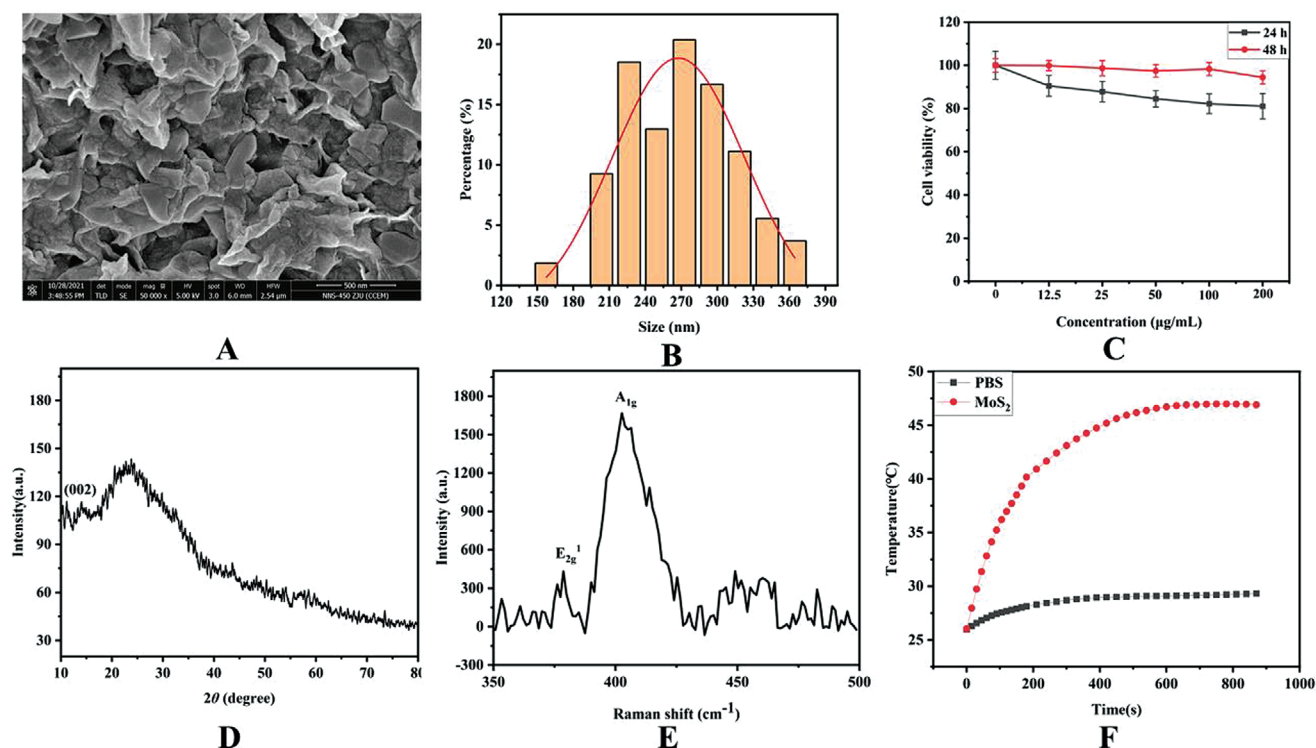


Figure 1. A) SEM, B) size distribution, C) cytotoxicity assay, D) XRD, E) Raman spectra, and F) photothermal heating curves of the MoS₂ nanosheets.

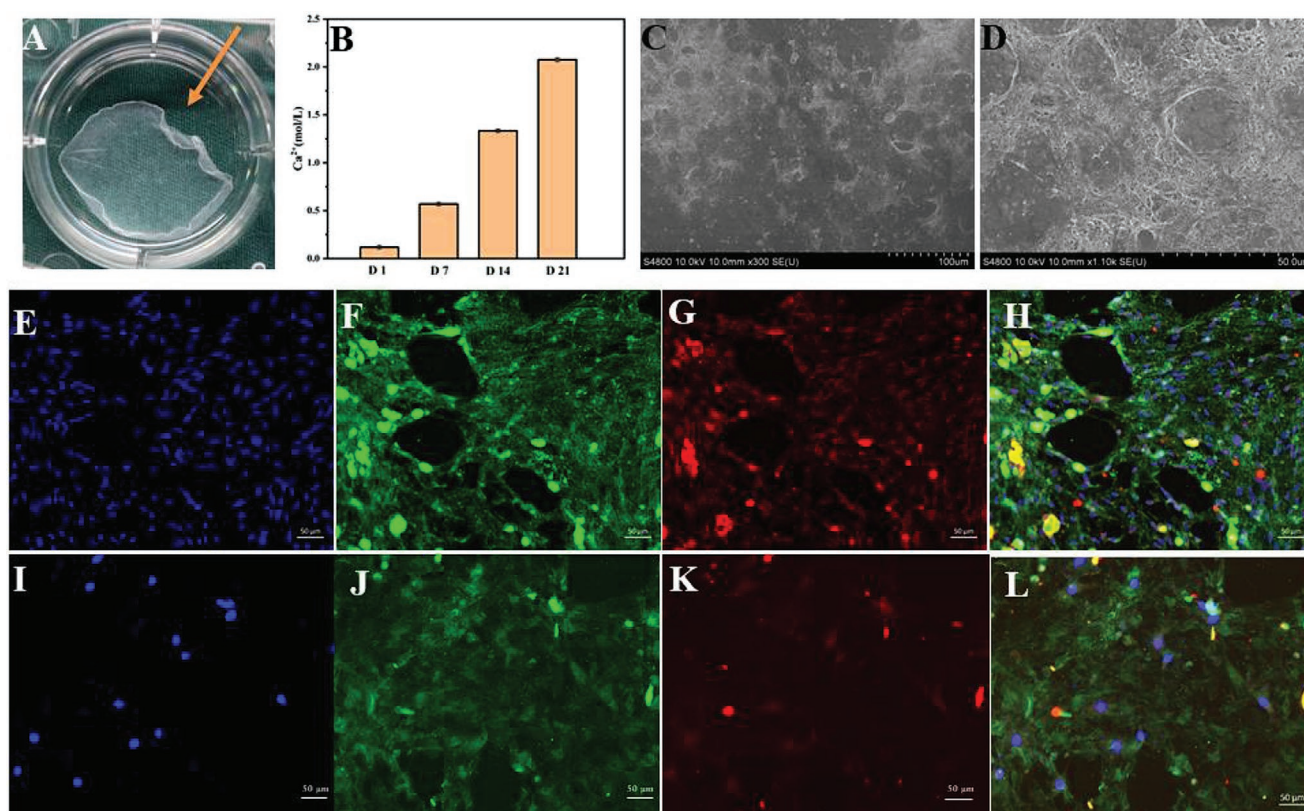


Figure 2. Characterization of OiECM. A) Optical image of OiECM in the 6-wells plates (yellow arrow point out the OiECM) and B) quantitative analysis of calcium in the OiECM after 1, 7, 14, and 21 days of culture. C) SEM image of the OiECM; scale bar: 100 μm . D) Enlarged SEM image of the OiECM; scale bar: 50 μm . DAPI (E), DiO (F), and collagen I immunofluorescent (G) staining of the cell nucleus of OiECM before decellularization. H) Merge fluorescent image of extracellular matrix. DAPI (I), DiO (J), and collagen I immunofluorescent (K) staining of the cell nucleus of OiECM after decellularization. L) Merge fluorescent image of extracellular matrix. (E–L) scale bar: 50 μm .

after they had undergone osteo-induction. As shown in **Figure 2A**, a thin white film-like layer, which was considered to be OiECM, was exfoliated from the edge of a petri dish and was allowed to float on the surface of the liquid (Movie S1, Supporting Information). The Ca^{2+} content of the BMMSCs increased with increase in osteo-induction time (Figure 2B), suggesting an increase in the degree of mineralization of OiECM. After careful analysis, we chose the OiECM culture time to be 21 Days. Analysis of SEM images showed that OiECM has a tough surface and 3D structure (Figure 2C,D).

Collagen I is widely distributed within the extracellular matrix. To evaluate the efficacy of the decellularization process, we used DAPI to stain any cell nucleus (blue fluorescence) present, DiO to stain cell membrane (green fluorescence), and collagen I immunofluorescent dye to stain the extracellular matrix (red fluorescence). The ECM was stained before (Figure 2E–H) and after the decellularization process (Figure 2I–L). Before decellularization, positive results after DAPI (Figure 2E, blue) and DiO (Figure 2F, green) staining was an indication that there were many cells adhered on the surface of ECM. After the decellularization process, there was still presence of red fluorescence (Figure 2K), but blue fluorescence could barely be seen (Figure 2I), an indication that there were very few cells adhered to the surface of ECM. These results demonstrated that we had succeeded in generating OiECM.

To investigate the effect of OiECM on the expression of osteogenic genes, rBMMSCs were seeded in petri dishes layered with OiECM. Cells seeded in petri dishes without the OiECM layer were used as controls. After 21 days, real-time PCR was used to assess the expression of osteogenic gene markers such as COL I, BMP-2, and OPN in rBMMSCs. As shown in **Figure 3**, the rBMMSCs cultured on OiECM had significantly higher gene expression levels of COL I, BMP-2, and OPN compared to the control groups at 21 days. These outcomes demonstrated that OiECM could significantly influence the expression of osteogenic genes in rBMMSCs in vitro. Consequently, we added OiECM to the PTEB to increase its osteo-induction ability.

2.1.3. Preparation and Characterizations of BAG/MoS₂-BAG/OiECM-MoS₂-BAG Scaffolds

We used porous BAG scaffolds as the main structure of the tissue-engineered bone. The BAG scaffolds are made of biotin, agarose, and gelatin, which are degradable and have excellent biocompatibility properties. We first combined the MoS₂ nanosheets and the BAG scaffolds to produce photothermal MoS₂-BAG scaffolds. Thereafter, we covered the scaffold using OiECM to generate OiECM-MoS₂-BAG Scaffolds.

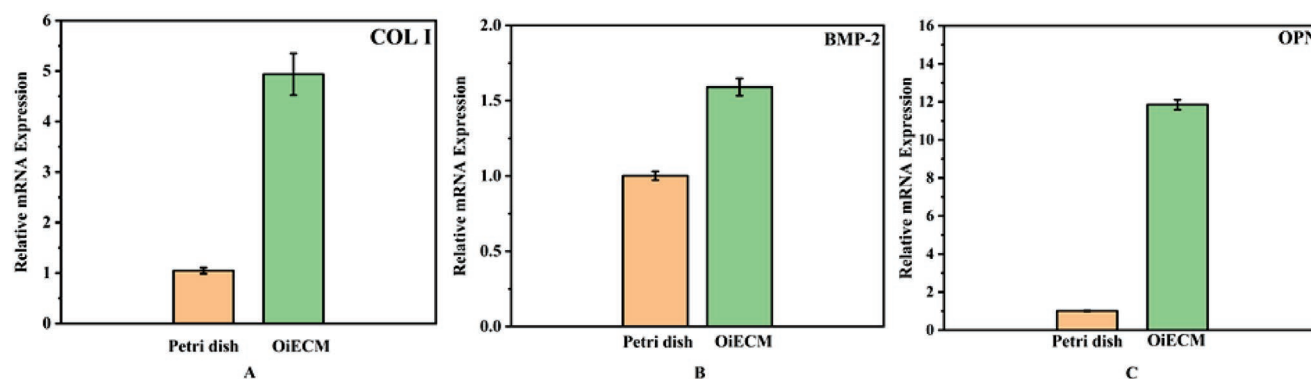


Figure 3. Gene expressions of Col I (A), BMP-2 (B), and OPN (C) proteins after rBMSCs culturing on a petri dish for 21 days.

As shown in Figure 3, the BAG scaffold was faint yellow, whereas the MoS₂-BAG was gray and OiECM-MoS₂-BAG scaffold was gray covered by a faint yellow membrane. All three groups of scaffolds exhibited a similar honeycomb structure. The SEM images showed the surface morphologies of the three scaffolds (Figure 4). Due to the addition of the MoS₂ nanosheets, the MoS₂-BAG scaffolds had a smaller pore size of $\approx 150\text{--}200\ \mu\text{m}$ (Figure 4B) when compared to the BAG groups scaffolds that had a pore size of $\approx 200\text{--}300\ \mu\text{m}$ (Figure 4A). As shown in Figure 4C, BAG scaffolds overlaid by a 5 μm thick white OiECM layer that forms a representative core/shell structure. The micro-CT images in Figure 4 reveals that only the OiECM-MoS₂-BAG scaffolds were covered by a mineralized OiECM layer.

The chemical compositions of the BAG, MoS₂-BAG, and OiECM-MoS₂-BAG scaffolds were characterized using XRD, Raman spectra, and FTIR spectroscopy. In X-ray diffraction (XRD) patterns of the MoS₂-BAG scaffold, the spectrum of gelatin presented a broad peak at 21° (Figure S2, Supporting Information), which can be attributed to its a helix and its triple-helical structure. Other peaks of MoS₂, like 002, 004, and 006 were also observed. In the Raman spectra of BAG scaffold (Figure S3, Supporting Information), the bands at 680 and 1065 cm⁻¹ (C–S) belonged to biotin. In the Raman spectra of MoS₂-BAG scaffold, the new band at 333 cm⁻¹ (J3) belonged to the MoS₂ nanosheets. In Raman spectra of OiECM-MoS₂-BAG scaffold, the bands at 890 (CN Ring), 1224 (–CH), 1234 (–CH₂), and 1434 cm⁻¹ Amide III belonged to OiECM. The FTIR spectroscopy of the BAG, MoS₂-BAG, and OiECM-MoS₂-BAG scaffolds are shown in Figure S4, Supporting Information. In FTIR spectroscopy of BAG and MoS₂-BAG scaffold, the bands at 1056 (C–C), 3261 (N–H), 1631 (Amide II), 2361 (C≡C), and 3500 cm⁻¹ (Amide A) belonged to the BAG scaffold. The new bands at 1621 (C=O) and 3105 cm⁻¹ carboxy group (O–H) belonged to OiECM.

Thereafter, we evaluated the porosity, water absorption, and water retention properties of the BAG, MoS₂-BAG, and OiECM-MoS₂-BAG Scaffolds. The BAG, MoS₂-BAG, and OiECM-MoS₂-BAG scaffolds exhibited a similar honeycomb structure with a porosity of $80.44 \pm 2.17\%$, $80.96 \pm 0.8\%$, and $71.35 \pm 2.93\%$, respectively (Figure S5, Supporting Information). A scaffold with high water absorption and retention capacity is desirable as it enhances the nutrient transfer

and cell proliferation. We found that the BAG, MoS₂-BAG, and OiECM-MoS₂-BAG scaffolds had high water absorption capacity approximately at $2146.3 \pm 219.18\%$, $2766.07 \pm 4.62\%$, and 2282.8 ± 4.75 , respectively (Figure S6, Supporting Information). The OiECM-MoS₂-BAG scaffolds showed highest water retention capacity among the three scaffolds at $\approx 93.5\%$ (Figure S7, Supporting Information).

2.1.4. Preparation of BTEB/MTEB/PTEB

We used rBMSCs as seeding cells in BAG, MoS₂-BAG and OiECM-MoS₂-BAG Scaffolds to form BAG tissue-engineered bone (BTEB), MoS₂-BAG tissue-engineered bone (MTEB), and PTEB, respectively.

2.2. Osteogenesis of PTEB

Thermotherapy, as well as therapeutic exercise, is widely used for the treatment of joint diseases such as OA and rheumatoid arthritis.^[39] However, application of thermotherapy 40–50 °C for 30 min to the skin and normal tissues may induce injury.^[40] According to reports, local hyperthermia at 41 °C for 15 min increased cell viability and metabolism, whereas thermotherapy at a temperature equal to, or higher than 43 °C reduced the viability and metabolic processes in chondrocyte-like cell line HCS-2/8.^[41] It was been reported that local hyperthermia at 42 °C for 15 min promoted bone deposition in critical-sized skull defects. It also mentioned that osteoblasts exposed to 42 °C, the cytoskeleton of osteoblasts would reassemble after incubation at 37 °C, but this reversible recovery did not occur at 45 °C or a higher temperature.^[42] In addition, it is necessary to use many heating cycles which can elicit any significant heat shock enhancement of osteogenesis.^[43] Thermotherapy at 41 °C was found to be the optimal temperature which effectively promoted the differentiation of hBMSCs into osteoblasts.^[44] Wang et al. reported that exposure to BPs@PLGA to NIR irradiation, at a constant temperature of $41 \pm 1\ ^\circ\text{C}$ for 450 s, effectively up-regulated the expression of heat shock proteins (HSP) thereby enhancing osteogenesis in vitro and in vivo.^[18] Therefore, PTEB under NIR radiation was applied to maintain a thermal effect for 10 min at 41 °C every week, after which the

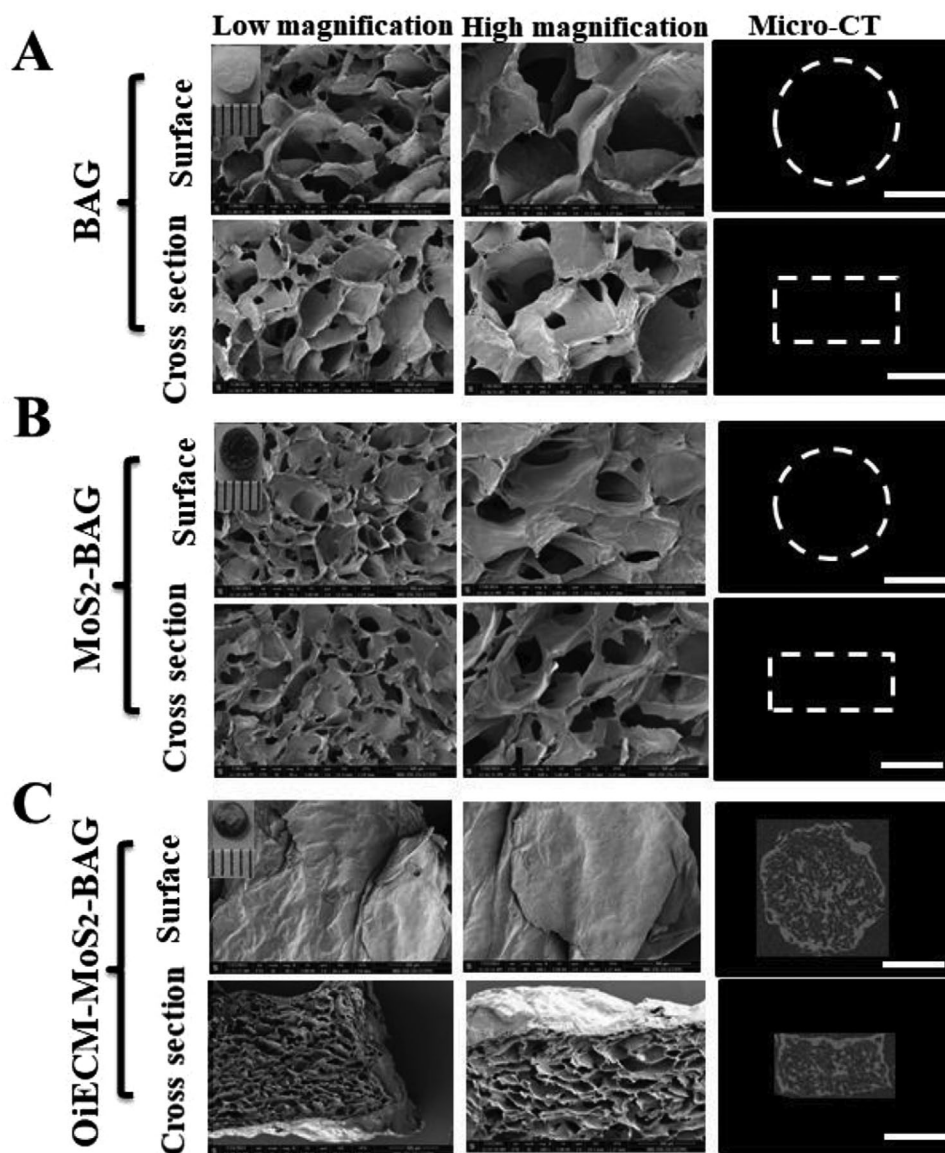


Figure 4. Characterization of the BAG/MoS₂-BAG/OiECM-MoS₂-BAG scaffolds. An optical image, SEM image, and micro-CT 3D reconstruction of A) BAG scaffold, B) MoS₂-BAG scaffold, and C) OiECM-MoS₂-BAG scaffold. Scale bar: low magnification: 200 μm, high magnification: 100 μm, micro-CT: 3 mm.

effect of this treatment on osteoblast differentiation and bone repair was examined.

2.2.1. Cell Compatibility of BTEB/MTEB/PTEB

We tested the cytotoxicity of BTEB, MTEB, PTEB, and PTEB under NIR radiation to ensure that all the tissue-engineered bones were safe. We assessed the cell survival rate of the rBMSCs after 1, 7, and 14-days incubation in the three bones using CCK-8 assay (Figure 5A). The results of CCK-8 assay were consistent with the results of live/dead staining (Figure 5C). As shown in Figure 5C, the rBMSCs cells adhered and proliferated on BTEB, MTEB, PTEB, and PTEB under NIR radiation. The PTEB and PTEB under NIR radiation groups showed better

cytocompatibility than the other groups. We then used SEM to observe the cells incubated with the different types of tissue-engineered bones for 14 days. More live cells were observed in the PTEB and PTEB under NIR radiation groups than in the BTEB and MTEB groups (Figure 5D). These results indicated that the PTEB and PTEB under NIR radiation groups were suitable for rBMSCs growth.

2.2.2. Evaluation of Osteogenic Differentiation

The most important sign of osteogenic differentiation is ALP activity. We tested the relative ALP activity of rBMSCs after 7 days of culture on BTEB, MTEB, PTEB, and PTEB under NIR radiation. As shown in Figure 5B, the PTEB under NIR

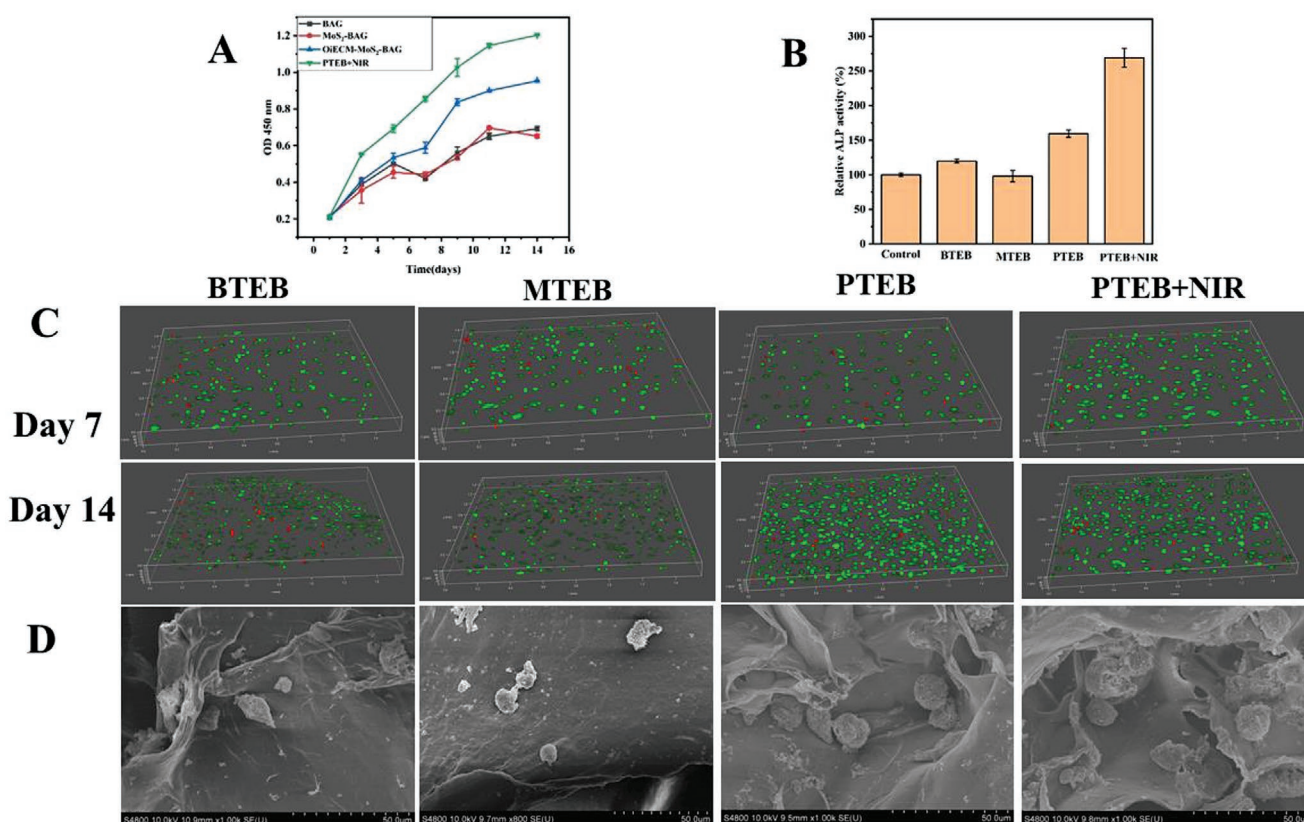


Figure 5. Cell viability and proliferation of the rBMSCs seeded on BTEB, MTEB, PTEB, and PTEB under NIR radiation. A) Cell proliferation curve at 1, 3, 5, 7, 9, 11, and 14-days incubation. B) Relative ALP activity of rBMSCs at 7-days culture. C) Live/dead staining of cells on scaffolds determined by the Calcein/PI assay at 7 and 14 days of culture (live cells: green and dead cells: red). D) SEM images of cells attached to the scaffold at 14-days incubation (yellow arrows: seeded rBMSCs). Scale bar: 50 μ m.

radiation group showed the highest ALP activity among all the other groups. This was an indication that the PTEB under NIR radiation group shows a high degree of osteogenic differentiation.

Moreover, we also assessed the presence of mineralized nodules using the Alizarin red S staining after incubation of rBMSCs on BTEB, MTEB, PTEB, and PTEB under NIR radiation for 21 days. As shown in **Figure 6**, the PTEB under the NIR radiation group had a higher number of mineralized nodules than the other groups, suggesting that the best mineralization of rBMSCs occurred when cultured on PTEB under NIR radiation. These results revealed that the microenvironment created by the PTEB under NIR radiation group can significantly promote the proliferation and differentiation of cultured rBMSCs. These results demonstrated that the group of PTEB under NIR radiation group had a higher degree of osteogenic differentiation.

2.3. In Vivo Bone Regeneration

2.3.1. Photothermal Conversion Ability of PTEB

Ground on the superior performance PTEB under NIR radiation promoting osteogenesis in vitro, we implant PTEB to

promote bone regeneration in vivo (**Figure 7A**). As shown in **Figure 7B**, PTEB showed great photothermal conversion ability under 808 nm radiation in vitro ($p = 1.2$ W). We established critical-size bone defect models in the cranial bones of male SD rats, and then implanted the different types of tissue-engineered bones into the bone defects to evaluate bone regeneration performances. To achieve this, we randomly divided 30 experimental rats (3-month, 300–400 g, male) into 5 groups; control, BTEB, MTEB, PTEB, and PTEB under NIR radiation groups. After the implantation procedure, the PTEB under NIR radiation group was put under weekly NIR radiation (1.5 W cm^{-2} , 600 s). We used an IR thermal imaging camera to record the photothermal effects during NIR irradiation in rats. The temperature of the PTEB + NIR group under 808 nm radiation ($p = 1.5$ W) rose from 32.7 to 41.0 $^{\circ}\text{C}$ in 120 s (**Figure 7C**). Under the same dense power NIR radiation, the maximum temperature of the BTEB under NIR radiation group was less than 36.5 $^{\circ}\text{C}$ after 600 s. This indicated that PTEB implantation under NIR radiation could penetrate the tissue and generate appropriate heat in vivo.

12-weeks after implantation, the rats were anesthetized and the skulls were harvested. The skulls were then fixed in 4% polyformaldehyde and the formation of new bone assessed using with micro-computed tomography (micro-CT) imaging and

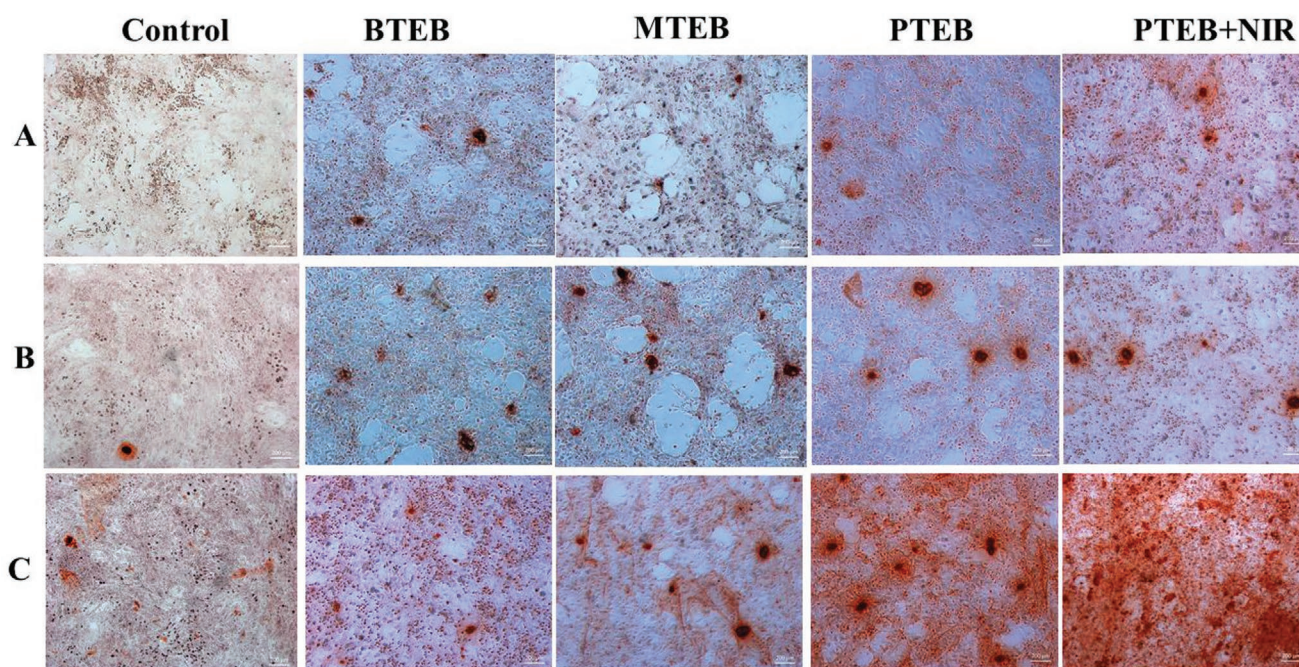


Figure 6. The Alizarin red S stained mineralized nodules after rBMSCs cell seeding on BTEB, MTEB, PTEB, and PTEB under NIR radiation groups at 7 (A), 14 (B), and 21 days (C) incubation. Scale bar: 200 μ m.

histological assays. Figure S8, Supporting Information, shows the images of the different types of tissue-engineered bones implanted into rat critical-size bone defects and the skull samples at 12 weeks post implantation.

2.3.2. Micro-CT Analysis

We utilized Micro-CT scanner to observe and quantitate the status of new bone growth 12 weeks after implantation. By

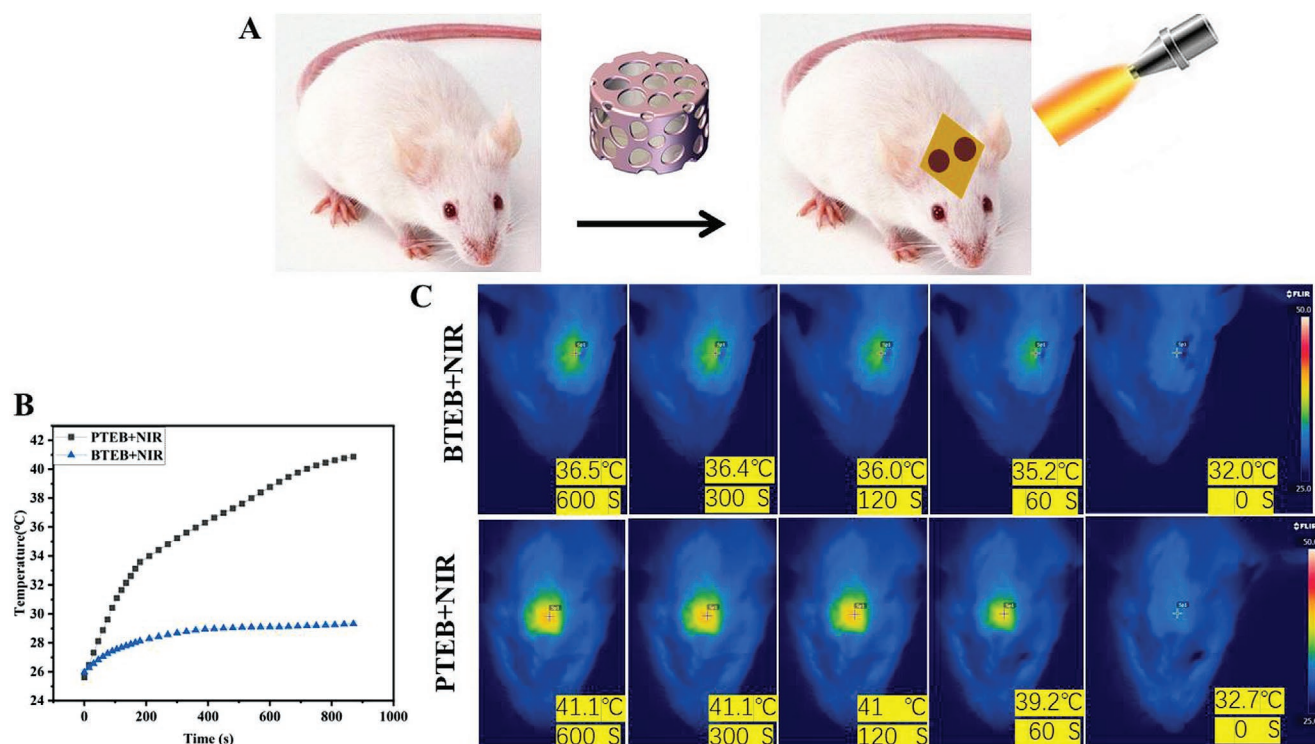


Figure 7. A) Schematic illustration of PTEB implantation and their repairing the critical-size bone defect model in rats. B) Photothermal conversion curves of BTEB and PTEB under 808 nm radiation in vitro ($p = 1.2$ W). C) IR thermal images of BTEB and PTEB under 808 nm radiation in rats ($p = 1.5$ W).

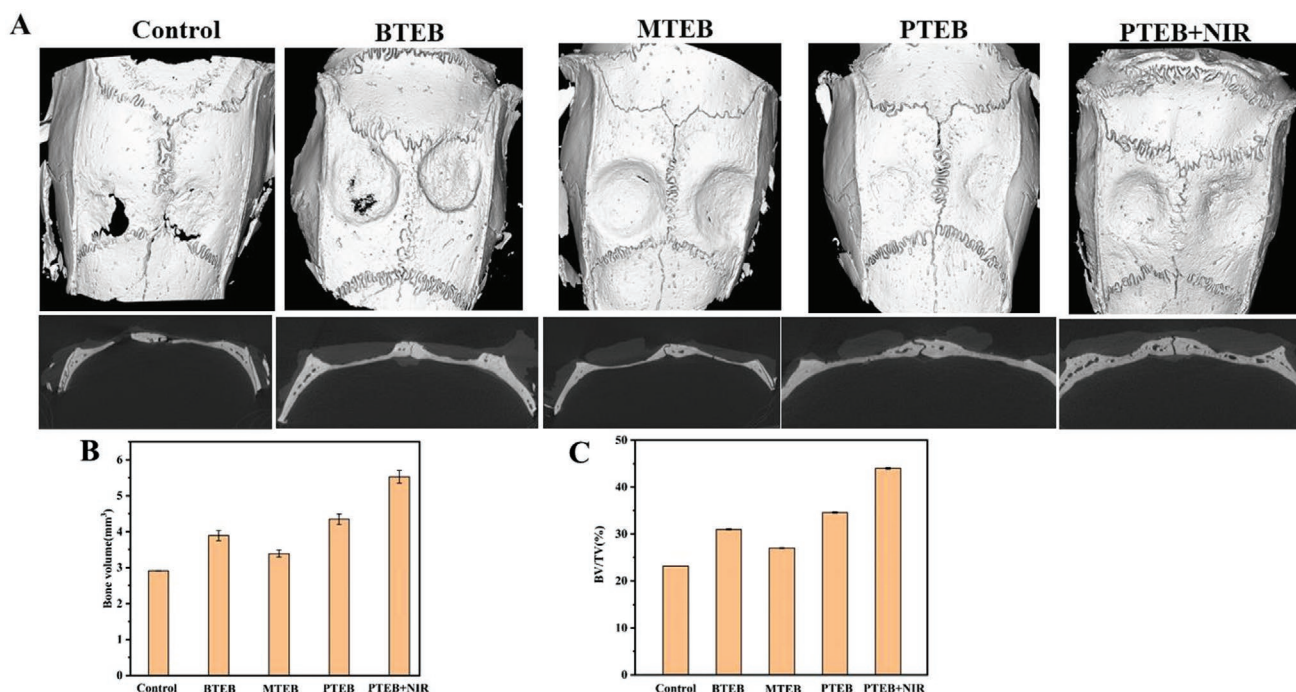


Figure 8. A) 3D reconstruction and sagittal images by Micro-CT analysis for control, BTEB, MTEB, PTEB, and PTEB under NIR radiation; B) bone value and C) BV/TV results by micro-CT for each group ($n = 3$).

combining micro-CT images and reconstructed 3D of micro-CT images, we saw that the PTEB under NIR radiation group had a better ability to repair critical-size bone defects than other groups (Figure 8). As shown in Figure 8, the presence of new bone tissue in the areas with defects was an indication that the scaffolds had been degraded and absorbed during the process of new bone formation. The PTEB under NIR radiation group showed excellent osteogenic performance and only a small amount of tissue-engineered bone remained when compared to other groups (Figure 8). We attributed this desirable therapeutic effect to the synergism between the osteo-induction properties of OiECM and the photothermal effects of the MoS₂ nanosheets. During the bone regeneration process, rBMSCs adhered and proliferated on the tissue-engineered bone, then initiated osteo conduction and osteo induction, and finally formed new bone on the vanishing tissue-engineered bone.

Moreover, we carried out quantitative analyses of the bone volume (BV) and the relative bone volume fraction (BV/TV) using the system-provided software. The micro-CT data in Figures 8B and 8C shows that the PTEB under NIR radiation group had the best post-operative bone volume (BV) (5.528 ± 0.969 mm³) and post-operative bone volume/tissue volume (BV/TV) ratio ($43.99 \pm 7.71\%$) among all the groups. These results indicated that there was better osteogenesis in the PTEB under NIR radiation group and that OiECM and MoS₂ nanosheets played important synergistic roles during bone regeneration.

2.3.3. Histological Analysis

The results of H&E staining and Masson's trichrome staining after 12 weeks showed that the PTEB under NIR radiation

group had a high amount of new bone. A thin fibrous tissue layer surrounding the old bone edge was observed in the control group, suggesting that no new bone had been generated in the defect during the 12-weeks of treatment. On the other hand, a small amount of new bone was generated in the defects of the BTEB, MTEB, and PTEB groups (Figure 9). In contrast, the new bone generated in the PTEB under NIR radiation group showed dense structure, which verified the outstanding bone regeneration performance of PTEB under NIR radiation. These results were consistent with results observed using micro-CT imaging (Figure 8B,C). The results suggested that the implantation of the novel PTEB can efficiently repair critical size bone defects in rats. They also showed that OiECM and the MoS₂ nanosheets worked synergistically to promote the process of osteo genesis. These findings have potential to revolutionize research in bone tissue engineering.

3. Conclusion

In summary, rat critical-sized cranial defects can be effectively repaired using PTEB under NIR radiation. The tissue-engineered bone was generated by overlaying the MoS₂-BAG scaffold with OiECM and then seeding the scaffold with rBMSCs. OiECM not only creates biomimetic cellular environments for rBMSCs, but it also has numerous cell-secreted growth factors that enhance cell growth and response. Hyperthermia-induced the up-regulation of protein expression has been shown to efficiently promote bone regeneration. The MoS₂ nanosheets in the PTEB acted as a photothermal agent and worked synergistically with OiECM, to promote bone regeneration. Using a critical-sized cranial defect in vivo model, we

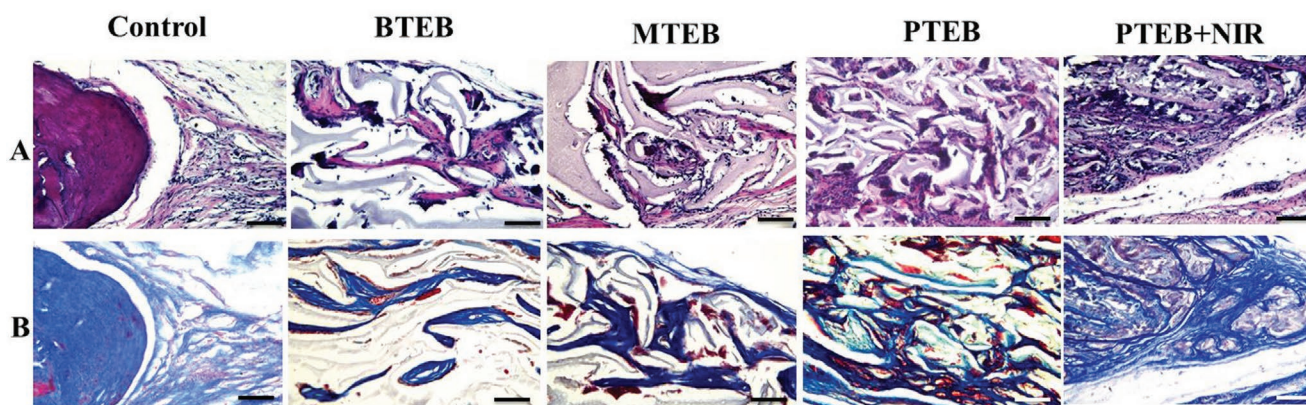


Figure 9. Images of H&E (A), Masson and Goldner (B) staining of the defects treated with control, BTEB, MTEB, PTEB, and PTEB under NIR radiation. Scale bar: 50 μm .

demonstrated that the PTEB under NIR radiation improved the regeneration of bone. Therefore, PTEB is a promising bone implantation in bone regenerative medicine.

4. Experimental Section

Materials: Biotin, gelatin, agarose, glutaric dialdehyde, and acetic acid were obtained from Aladdin, (Shanghai, China), while Alizarin red, DiO, PBS, oil red O, and safranin O were purchased from Beyotime Biotechnology Co., Ltd (Shanghai, China). Fetal bovine serum (FBS) and low glucose Dulbecco's modified Eagle's medium (DMEM) were obtained from Hyclone (Logan, USA). Calcium quantitative assay kit, DAPI, Trizol reagent, Revert Aid First Strand cDNA Synthesis Kit, KAPA SYBR FAST qPCR Kit Master Mix, hematoxylin and eosin (H&E), Masson's trichrome, LIVE/DEAD assay kit (fluorescein diacetate [FDA, green] and propidium iodide [PI, red]), trypsin, the alkaline phosphatase activity (ALP) microplate test kit were purchased from Sangon (Shanghai, China). All reagents were used as received without further purification.

Sample Characterizations: The MoS_2 nanosheets were observed using TEM (Tecnai G2 spirit, FEI, USA) at a voltage of 120 kV, while the scaffolds and PTEBs were observed using SEM (Nova Nano 450, FEI, USA) at a voltage of 20 kV. The X-ray diffraction (D8 ADVANCE, Bruker, Germany) patterns were obtained using a D/max-2500 system with a $\text{Cu K}\alpha$ radiation ($\lambda = 0.154 \text{ nm}$) at a scan rate of $10^\circ \text{ min}^{-1}$. The FTIR spectroscopy was acquired using an (IRAffinity-1, Shimadzu, Japan), while the Raman scattering spectra analysis was carried out using a visible high-resolution confocal Raman microscope (in Via Reflex, Renishaw, England) equipped with 532 and 785 nm laser. The mineralization of BAG/ MoS_2 -BAG/OiECM- MoS_2 -BAG scaffolds was assessed using micro-CT U-CT-XUHR (Milabs, Netherlands). Laser scanning confocal microscopy (LEICA, SP8, Japan). Real-time PCR analysis was carried out using Prism 7900HT from ABI (Texas, USA). To evaluate the photothermal performance of the BAG/ MoS_2 -BAG/OiECM- MoS_2 -BAG scaffolds, an 808 nm NIR laser with a power density of 1.5 W cm^{-2} was employed and the temperature changes were recorded using a Ti27 infrared thermal imaging camera (micro-LIF, LaVision GmbH, Germany). The 808 nm NIR laser was purchased from Changchun New Industry Photoelectric Technology Co. LTD.

Sample Fabrication of PTEB^[37]: MoS_2 (2 g) powder was added to 15 mL of N-methylpyrrolidone and stirred for 25 min. The mixture was then sonicated in an ice-water bath for 50 min, followed by centrifugation at 2000 rpm for 30 min. The precipitate was washed with isopropanol and bath sonicated for 10 min to remove the N-methylpyrrolidone. The MoS_2 nanosheets obtained were stored at 4°C until further use.

The MoS_2 -BAG scaffolds were prepared by first dissolving 100 mg biotin and 100 mg gelatin in 7 mL 1% aqueous acetic acid solution to make A solution. The authors then dissolved 200 mg agarose and 8 mg MoS_2 nanosheets in 5 mL hot water to make B solution. Thereafter, 0.5 mL 0.2% [v/v] glutaraldehyde was added to a mixture of A and B solution, and then the solution mixture was poured into an acrylic container and incubated at -20°C for 12 h, to form porous MoS_2 -BAG scaffold. The BAG scaffolds were prepared in a similar manner but without the addition of MoS_2 nanosheets.

The authors cultured rat BMMSCs at passage 3 in osteo-induced culture medium for 21 days and then carried out a decellularization to obtain OiECM. The OiECM was stored at -20°C until further use. Decellularization efficiency was assessed by staining OiECM with DAPI, DiO, and collagen-I and observing the samples under a fluorescence microscope. Thereafter, the secretion of calcium ion on the matrix was evaluated at 0, 7, 14, and 21 days using the calcium quantitative assay kit.

The rat BMMSCs were isolated from bone marrow cavities based on a previously published protocol.^[45] The rat BMMSCs was passaged every 3 days and their potential for trilineage differentiation into chondrogenic, osteogenic, and adipogenic lineages was assessed as previously described. They examined the chondrogenic, osteogenic, and adipogenic capacities of the rat BMMSCs to assess its trilineage differentiation potential as previously described. Osteogenic induction was carried out by culturing rat BMMSCs at passage 3 in osteo-induced culture medium for 2 weeks. Thereafter, mineralization of rat BMMSCs was analyzed using Alizarin Red staining. Adipogenic induction was carried out by culturing passage 3 rat BMMSCs at passage 3 in adipogenic differentiation culture medium for 3 weeks. The presence of lipid vacuoles was determined using Oil red O staining for the detection of lipids vacuoles. Chondrogenic differentiation was carried out by culturing rat BMMSCs at passage 3 in a chondrogenic induced medium for 4 weeks. Chondrogenic differentiation was analyzed using toluidine blue staining.

Real-time polymerase chain reaction (RT-PCR) was used to analyze the expression levels of osteogenesis-related genes in rat BMMSCs. TRIzol Reagent was used to isolate total RNA, followed by reverse transcription of the RNA to generate complementary DNA (cDNA) according to the PrimeScript reagent Kit with gDNA Eraser (Takara). Finally, RT-PCR was performed using TB Green Premix Ex Taq (Takara) according to manufacturer's instructions (Takara). These gene expressions were obtained after normalization against the cycle threshold value of the housekeeping gene (GAPDH). Five samples in each group were used for RT-PCR analysis. The sequences of the primers used in this study are listed below:

GAPDH forward 5'- CGCTAACATCAATGGGGTG-3';
GAPDH reverse 5'- TTGCTGACAATCTTGAGGGAG-3';

BMP-2 forward 5'-AACGAGAAAAGCGTCAAGCC-3';
BMP-2 reverse 5'-CCAGTCATTCCACCCACA-3';
COL I forward 5'-GACCTCAAGATGTCCACT-3';
COL I reverse 5'-GAACCTTCGCTTCCATACTCG-3';
OPN forward 5'-TTGGCTTTGCAGTCTCTCGCG-3';
OPN reverse 5'-AGGCAAGGCCGAACAGGCAAA-3';

Rat BMMSCs were seeded on MoS₂-BAG scaffolds to form MoS₂ tissue-engineered bone (MTEB). Thereafter, the sterilized MTEB was put in the middle of the OiECM membrane and wrapped carefully using tweezers (Movie S1, Supporting Information). One piece of OiECM collected from one 6-wells plate was used to wrap one MTEB to form PTEB. The BTEB was prepared by seeding rat BMMSCs on BAG scaffold.

The parameters of the different types of scaffolds were recorded before and after soaking in ethanol for 10 min. The weight of the scaffolds was recorded before and after soaking in deionized water at room temperature for 24 h as well as before and after centrifugation. The authors then calculated the porosity, water absorption, and retention ratio of the scaffolds as previously reported.

Osteogenesis of PTEB: BTEB, MTEB, PTEB, and PTEB under NIR radiation were cultured with rats BMMSCs for 14 days. During this period, the PTEB under NIR radiation group was irradiated under 808 nm NIR laser every 3 days. SEM was used to assess the cytomorphology of cells attached on the PTEB. Thereafter, the viability of rat BMMSCs cultured on the different scaffolds was evaluated at 1, 7, and 14 days using the CCK-8 assay.

To assess the ability of PTEB to promote osteogenesis of BMMSCs, rat BMMSCs were cultured with PTEB under NIR radiation. Osteogenic differentiation of rat BMMSCs was estimated using the ALP activity at 7 days. Alizarin red staining was used to investigate the osteogenesis of rat BMMSCs after culturing in osteogenic medium for 21 days.

In Vivo Examination of Critical Size Defects: The SD rats were reared in an animal laboratory center under SPF conditions. All the animal procedures and experiments were carried out humanely under sterile conditions, and were approved by the Ethics Committee for Animal Research, Zhejiang Academy of Medical Sciences (ZJCLA-IACUC-20040017). To generate a critical-size defect model, the authors used a 5 mm dental drill to create two critical and cylindrical defects in the middle of the skulls of 30 experimental rats (3-month old, 300–400 g, male), and then closed the wounds carefully. Thereafter, the rats were randomly divided into 5 groups as Group 1: no implantation, Group 2: BTEB implantation, Group 3: MTEB implantation, Group 4: PTEB implantation, and Group 5: PTEB implantation under weekly NIR radiation (1.5 W cm⁻², 600 s) post-surgery. NIR radiation was carried out in anesthetized and fixed rats. After 12-weeks, the rats were anesthetized and their skulls isolated and fixed in 4% polyformaldehyde to observe new bone formation using micro-computed tomography (micro-CT) imaging and histological assays.

New bone formation was assessed by observing the samples using a micro-CT scanner and reconstructing the images using the system-provided software. The authors also analyzed the relative bone volume fraction (BV/TV) and the bone volume using system-provided software.

After carrying out micro-CT, the skulls were demineralized using EDTA decalcifying solution. The areas with new bone formation were stained with Hematoxylin-Eosin and Masson, and then observed under an optical microscope for histological analysis.

Supporting Information

Supporting Information is available from the Wiley Online Library or from the author.

Acknowledgements

J.Z. and B.Z. contributed equally to this work. This work was supported by Medical and Health Science and Technology Program of Zhejiang

Province 2021RC085 (L.W.), Zhejiang Provincial Program for the Cultivation of High-level Innovative Health talents 2016-6 (Q.S.), and the National Science Foundation of China 21874038 (Q.C.). This work also was supported by Jiagen Lv of the Shaanxi Normal University. We also thank Dandan Song in center of Cryo-Electron Microscopy (CCEM), Zhejiang University for her technical assistance on Scanning Electron Microscopy.

Conflict of Interest

The authors declare no conflict of interest.

Data Availability Statement

The data that support the findings of this study are available from the corresponding author upon reasonable request.

Keywords

bone regeneration, critical-size bone defects, extracellular matrix, NIR radiation, photothermal

Received: September 29, 2021

Revised: November 18, 2021

Published online:

- [1] Y. Zha, Y. Li, T. Lin, J. Chen, S. Zhang, J. Wang, *Theranostics* **2021**, *11*, 397.
- [2] W. Qiao, K. H. M. Wong, J. Shen, W. Wang, J. Wu, J. Li, Z. Lin, Z. Chen, J. P. Matinlinna, Y. Zheng, S. Wu, X. Liu, K. P. Lai, Z. Chen, Y. W. Lam, K. M. C. Cheung, K. W. K. Yeung, *Nat. Commun.* **2021**, *12*, 2885.
- [3] M. Zhu, W. Li, X. Dong, X. Yuan, A. C. Midgley, H. Chang, Y. Wang, H. Wang, K. Wang, P. X. Ma, H. Wang, D. Kong, *Nat. Commun.* **2019**, *10*, 4620.
- [4] C. Zhu, J. Lin, H. Jiang, J. Gao, M. Gao, B. Wu, W. Lin, G. Huang, Z. Ding, *Cell Tissue Res.* **2021**, *385*, 639.
- [5] J. Lee, A. Sutani, R. Kaneko, J. Takeuchi, T. Sasano, T. Kohda, K. Ihara, K. Takahashi, M. Yamazoe, T. Morio, T. Furukawa, F. Ishino, *Nat. Commun.* **2020**, *11*, 4283.
- [6] B. A. Dikici, G. C. Reilly, F. Claeysens, *ACS Appl. Mater. Interfaces* **2020**, *12*, 12510.
- [7] Y. Lu, Y. Wang, H. Zhang, Z. Tang, X. Cui, X. Li, J. Liang, Q. Wang, Y. Fan, X. Zhang, *ACS Appl. Mater. Interfaces* **2021**, *13*, 24553.
- [8] H. S. Kim, N. Mandakhbayar, H.-W. Kim, K. W. Leong, H. S. Yoo, *Biomaterials* **2021**, *269*, 120214.
- [9] C. Black, J. M. Kanczler, M. C. de Andrés, L. J. White, F. M. Savi, O. Bas, S. Saifzadeh, J. Henkel, A. Zannettino, S. Gronthos, M. A. Woodruff, D. W. Huttmacher, R. O. C. Oreffo, *Biomaterials* **2020**, *247*, 119998.
- [10] B. L. Seal, A. Panitch, *Encyclopedia of Medical Devices and Instrumentation*, John Wiley & Sons, Ltd, New York **2006**.
- [11] C. He, L. Yu, H. Yao, Y. Chen, Y. Hao, *Adv. Funct. Mater.* **2021**, *31*, 2006214.
- [12] H. Xiang, Q. Yang, Y. Gao, D. Zhu, S. Pan, T. Xu, Y. Chen, *Adv. Funct. Mater.* **2020**, *30*, 1909938.
- [13] S. Dong, Y. Chen, L. Yu, K. Lin, X. Wang, *Adv. Funct. Mater.* **2020**, *30*, 1907071.
- [14] X. Wang, B. Ma, J. Xue, J. Wu, J. Chang, C. Wu, *Nano Lett.* **2019**, *19*, 2138.

- [15] A. Marino, S. Arai, Y. Hou, A. Degl'Innocenti, V. Cappello, B. Mazzolai, Y.-T. Chang, V. Mattoli, M. Suzuki, G. Ciofani, *ACS Nano* **2017**, *11*, 2494.
- [16] C. Shui, A. Scutt, *J. Bone Miner. Res.* **2001**, *16*, 731.
- [17] Y. Wang, X. Hu, L. Zhang, C. Zhu, J. Wang, Y. Li, Y. Wang, C. Wang, Y. Zhang, Q. Yuan, *Nat. Commun.* **2019**, *10*, 2829.
- [18] L. Tong, Q. Liao, Y. Zhao, H. Huang, A. Gao, W. Zhang, X. Gao, W. Wei, M. Guan, P. K. Chu, H. Wang, *Biomaterials* **2019**, *193*, 1.
- [19] B. Geng, H. Qin, W. Shen, P. Li, F. Fang, X. Li, D. Pan, L. Shen, *Chem. Eng. J.* **2020**, *383*, 123102.
- [20] W. Dang, T. Li, B. Li, H. Ma, D. Zhai, X. Wang, J. Chang, Y. Xiao, J. Wang, C. Wu, *Biomaterials* **2018**, *160*, 92.
- [21] T. Wang, S. Wang, Z. Liu, Z. He, P. Yu, M. Zhao, H. Zhang, L. Lu, Z. Wang, Z. Wang, W. Zhang, Y. Fan, C. Sun, D. Zhao, W. Liu, J.-C. G. Bünzli, F. Zhang, *Nat. Mater.* **2021**, *20*, 1571.
- [22] W. Tao, X. Ji, X. Xu, M. A. Islam, Z. Li, S. Chen, P. E. Saw, H. Zhang, Z. Bharwani, Z. Guo, J. Shi, O. C. Farokhzad, *Angew. Chem., Int. Ed.* **2017**, *56*, 11896.
- [23] X. Chen, C. Bartlam, V. Lloret, N. Moses Badlyan, S. Wolff, R. Gillen, T. Stimpel-Lindner, J. Maultzsch, G. S. Duesberg, K. C. Knirsch, A. Hirsch, *Angew. Chem., Int. Ed.* **2021**, *60*, 13484.
- [24] M. Cao, R. Cai, L. Zhao, M. Guo, L. Wang, Y. Wang, L. Zhang, X. Wang, H. Yao, C. Xie, Y. Cong, Y. Guan, X. Tao, Y. Wang, S. Xu, Y. Liu, Y. Zhao, C. Chen, *Nat. Nanotechnol.* **2021**, *16*, 708.
- [25] S. Karunakaran, S. Pandit, B. Basu, M. De, *J. Am. Chem. Soc.* **2018**, *140*, 12634.
- [26] J. K. Carrow, K. A. Singh, M. K. Jaiswal, A. Ramirez, G. Lokhande, A. T. Yeh, T. R. Sarkar, I. Singh, A. K. Gaharwar, *Proc. Natl. Acad. Sci. USA* **2020**, *117*, 13329.
- [27] I. R. Suhito, Y. Han, D.-S. Kim, H. Son, T.-H. Kim, *Biochem. Biophys. Res. Commun.* **2017**, *493*, 578.
- [28] G. Sun, S. Yang, H. Cai, Y. Shu, Q. Han, B. Wang, Z. Li, L. Zhou, Q. Gao, Z. Yin, *J. Colloid Interface Sci.* **2019**, *549*, 50.
- [29] S. Ke, Y. Lai, L. Li, L. Tu, Y. Wang, L. Ren, S. Ye, P. Yang, *ACS Biomater. Sci. Eng.* **2019**, *5*, 1057.
- [30] S. Wu, J. Wang, L. Jin, Y. Li, Z. Wang, *ACS Appl. Nano Mater.* **2018**, *1*, 337.
- [31] H. Wang, X. Zeng, L. Pang, H. Wang, B. Lin, Z. Deng, E. L. X. Qi, N. Miao, D. Wang, P. Huang, H. Hu, J. Li, *Chem. Eng. J.* **2020**, *396*, 125081.
- [32] G. P. Awasthi, V. K. Kaliannagounder, B. Maharjan, J. Y. Lee, C. H. Park, C. S. Kim, *Mater. Sci. Eng., C* **2020**, *116*, 111162.
- [33] C. Stüdle, Q. Vallmajó-Martín, A. Haumer, J. Guerrero, M. Centola, A. Mehrkens, D. J. Schaefer, M. Ehrbar, A. Barbero, I. Martin, *Biomaterials* **2018**, *171*, 219.
- [34] E. M. Czekanska, J. Geng, M. Glinka, K. White, J. Kanczler, N. D. Evans, R. O. C. Oreffo, M. Bradley, *J. Mater. Chem. B* **2018**, *6*, 4437.
- [35] Z. Feng, J. Liu, C. Shen, N. Lu, Y. Zhang, Y. Yang, F. Qi, *Exp. Ther. Med.* **2016**, *11*, 737.
- [36] C. Lee, H. Yan, L. E. Brus, T. F. Heinz, J. Hone, S. Ryu, *ACS Nano* **2010**, *4*, 2695.
- [37] A. O'Neill, U. Khan, J. N. Coleman, *Chem. Mater.* **2012**, *24*, 2414.
- [38] S. Jiménez Sandoval, D. Yang, R. F. Frindt, J. C. Irwin, *Phys. Rev. B* **1991**, *44*, 3955.
- [39] K. A. Takahashi, H. Tonomura, Y. Arai, R. Terauchi, K. Honjo, N. Hiraoka, T. Hojo, T. Kunitomo, T. Kubo, *Int. J. Hyperthermia* **2009**, *25*, 661.
- [40] L. F. Fajardo L-G, *CancerResearch* **1984**, *44*, 4826s.
- [41] T. Hojo, M. Fujioka, G. Otsuka, S. Inoue, U. Kim, T. Kubo, *J. Orthop. Sci.* **2003**, *8*, 396.
- [42] S. Li, S. Chien, P.-I. Brånemark, *J. Orthop. Res.* **1999**, *17*, 891.
- [43] C. L. Lim, C. Byrne, J. K. Lee, *Ann. Acad. Med. Singapore* **2008**, *37*, 347.
- [44] J. Chen, Z.-D. Shi, X. Ji, J. Morales, J. Zhang, N. Kaur, S. Wang, *Tissue Eng., Part A* **2013**, *19*, 716.
- [45] S. Liu, S. Mou, C. Zhou, L. Guo, A. Zhong, J. Yang, Q. Yuan, J. Wang, J. Sun, Z. Wang, *ACS Appl. Mater. Interfaces* **2018**, *10*, 42948.